

## MILLIMETER MAPPING AT $z \sim 1$ : DUST-OBSCURED BULGE BUILDING AND DISK GROWTH

ERICA J. NELSON<sup>1,2</sup>, KEN-ICHI TADAKI<sup>3</sup>, LINDA J. TACCONI<sup>1</sup>, DIETER LUTZ<sup>1</sup>, NATASCHA M. FÖRSTER SCHREIBER<sup>1</sup>, ANNA CIBINEL<sup>4</sup>, STIJN WUYTS<sup>5</sup>, PHILIPP LANG<sup>6</sup>, MIREIA MONTES<sup>7,8</sup>, PASCAL A. OESCH<sup>9</sup>, SIRIO BELLÌ<sup>1</sup>, REBECCA L. DAVIES<sup>1</sup>, RICHARD I. DAVIES<sup>1</sup>, REINHARD GENZEL<sup>1</sup>, MAGDALENA LIPPA<sup>1</sup>, SEDONA H. PRICE<sup>1</sup>, HANNAH ÜBLER<sup>1</sup>, EMILY WISNIOSKI<sup>10</sup>

Submitted to *ApJ*

### ABSTRACT

A randomly chosen star in today's Universe is most likely to live in a galaxy with a stellar mass between that of the Milky Way and Andromeda. Yet it remains uncertain how the structural evolution of these bulge-disk systems proceeded. Most of the unobscured star formation we observe building Andromeda progenitors at  $0.7 < z < 1.5$  occurs in disks, but  $\gtrsim 90\%$  of their star formation is reprocessed by dust and remains unaccounted for. Here we map rest-500 $\mu\text{m}$  dust continuum emission in an Andromeda progenitor at  $z = 1.25$  to probe where it is growing through dust-obscured star formation. Combining resolved dust measurements from the NOEMA interferometer with Hubble Space Telescope  $H\alpha$  maps and multicolor imaging (including new UV data from the HDUV survey), we find a bulge growing by dust-obscured star formation: while the unobscured star formation is centrally suppressed, the dust continuum is centrally concentrated, filling in the ring-like structures evident in the  $H\alpha$  and UV emission. Reflecting this, the dust emission is more compact than the optical/UV tracers of star formation with  $r_e(\text{dust}) = 3.4\text{kpc}$ ,  $r_e(H\alpha)/r_e(\text{dust}) = 1.4$ , and  $r_e(\text{UV})/r_e(\text{dust}) = 1.8$ . Crucially, however, the bulge and disk of this galaxy are building simultaneously; although the dust emission is more compact than the rest-optical emission ( $r_e(\text{optical})/r_e(\text{dust}) = 1.4$ ), it is somewhat less compact than the stellar mass ( $r_e(M_*)/r_e(\text{dust}) = 0.9$ ). Taking the rest-500 $\mu\text{m}$  emission as a tracer of star formation, the expected structural evolution of this galaxy can be accounted for by star formation: it will grow in size by  $\Delta r_e/\Delta M_* \sim 0.3$  and central surface density by  $\Delta \Sigma_{\text{cen}}/\Delta M_* \sim 0.9$ . Finally, our observations are consistent with a picture in which merging and disk instabilities drive gas to the center of galaxies, boosting global star formation rates above the main sequence and building bulges.

*Subject headings:* galaxies: evolution — galaxies: structure — galaxies: star formation — dust

### 1. INTRODUCTION

Owing to significant investments in optical and near-infrared instrumentation, we now have high resolution mapping of large numbers galaxies in the rest-UV+optical during the epoch when they formed most of their stars ( $1 < z < 3$ ). This mapping has shown that most star formation as traced by  $H\alpha$  and UV emission occurs in clumpy, rotating galactic disks (e.g. Genzel et al. 2006; Genzel et al. 2008; Förster Schreiber et al. 2006, 2009; Wisnioski et al. 2011; Kassin et al. 2012; Wuyts et al. 2013; Nelson et al. 2013; Wisnioski et al. 2015; Stott et al. 2016). Additionally, studies mapping where galaxies are growing via rest-UV/optical tracers of the specific star formation rate ( $sSFR = SFR/M_*$ ) which trace present star formation relative to the integral of past star

formation (e.g. EW( $H\alpha$ ), UV-optical color gradients) typically find either flat or somewhat centrally depressed  $sSFR$ , meaning galaxies are generally growing somewhere between self-similarly, and inside-out; not, on average, getting more compact (Wuyts et al. 2012; Nelson et al. 2012; Nelson et al. 2013; Nelson et al. 2016b; Liu et al. 2016, 2017). However, a significant fraction of star formation is attenuated by dust and may be missed by these types of observations. Most importantly, this hampers our ability to determine where within galaxies most of the stars were formed and consequently how galaxies grew through star formation.

Recent studies of the spatially-resolved Balmer decrements, colors, and spectral energy distributions (SEDs) of large samples of galaxies have found that with increasing stellar mass, both the normalization and gradient in dust attenuation increases (e.g. Wuyts et al. 2012; Nelson et al. 2016a; Liu et al. 2016, 2017; Wang et al. 2017). At a most basic level, this suggests that the dust-obscured star formation may be distributed differently than the unobscured star formation in massive galaxies. In particular, it may be more compact. In massive galaxies near the peak of the cosmic star formation history ( $M_* \gtrsim 2 \times 10^{10} M_\odot$  at  $z \sim 1-2$ ), typically  $\gtrsim 90\%$  of the emission from star formation is absorbed by dust and re-radiated in the infrared (IR) (e.g. Reddy et al. 2006, 2010; Whitaker et al. 2012; Wuyts et al. 2011; Whitaker et al. 2014; Reddy et al. 2017). Thus, to determine how galaxies are building, it is essential to be able to map not only the unobscured star formation but also the obscured star formation. This has been difficult because telescopes operating at the far-IR (FIR) wavelengths necessary to probe the peak of the dust emission have had insufficient sensitivity and spatial resolution to map

<sup>1</sup> Max-Planck-Institut für extraterrestrische Physik, Giessenbachstrasse, D-85748 Garching, Germany

<sup>2</sup> Harvard-Smithsonian Center for Astrophysics, 60 Garden St, Cambridge, MA 02138, USA

<sup>3</sup> National Astronomical Observatory of Japan, 2-21-1 Osawa, Mitaka, Tokyo 181-8588, Japan

<sup>4</sup> Astronomy Centre, Department of Physics and Astronomy, University of Sussex, Brighton, BN1 9QH, UK

<sup>5</sup> Department of Physics, University of Bath, Claverton Down, Bath, BA2 7AY, UK

<sup>6</sup> Max Planck Institute for Astronomy (MPIA), Königstuhl 17, 69117, Heidelberg, Germany

<sup>7</sup> School of Physics, University of New South Wales, Sydney, NSW 2052, Australia

<sup>8</sup> Astronomy Department, Yale University, New Haven, CT 06511, USA

<sup>9</sup> Observatoire de Genève, 51 Ch. des Maillettes, 1290 Versoix, Switzerland

<sup>10</sup> Research School of Astronomy & Astrophysics, Australian National University, Canberra, ACT-2611, Australia

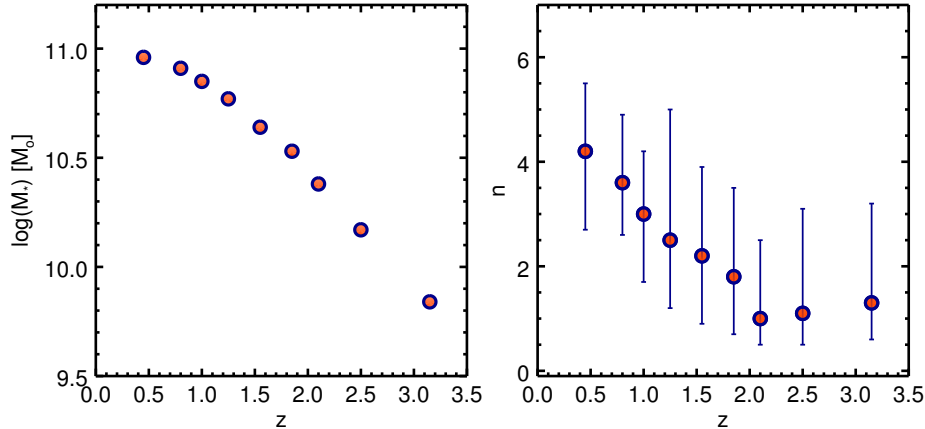


FIG. 1.— Left: Average stellar mass evolution of galaxies with present-day mass of the Andromeda based on abundance matching (Moster et al. 2013; Behroozi et al. 2013). In this paper we select a galaxy that based on its stellar mass is likely to be a  $z \sim 1$  progenitor of a galaxy with present-day mass similar to Andromeda (e.g. Papovich et al. 2015). Right: The evolution of the  $H_{F160W}$  Sérsic indices with time (Papovich et al. 2015). The steady increase in the Sérsic indices during the epoch of this study suggests that this is a critical epoch for understanding the growth of galactic bulges.

galaxies at  $z \sim 1-3$ .

With the increased sensitivity and spatial resolution of mm/submm interferometers such as NOEMA and ALMA, we can now map the dust continuum emission at longer wavelengths, however. For galaxies near the peak of the cosmic SFH at  $1 < z < 3$ , these interferometers can be used to efficiently probe dust continuum emission at rest-wavelengths  $\sim 200-500 \mu\text{m}$ . As the emission at these wavelengths represents thermal emission from dust largely heated by star formation for the rapidly star forming galaxies at this epoch, it has been used as tracer of obscured star formation (modulo dust temperature gradients) (e.g. Barro et al. 2016; Tadaki et al. 2017). A number of individual galaxies have now been mapped at millimeter wavelengths revealing in a significant fraction very centrally concentrated molecular gas and dust (e.g. Tacconi et al. 2008, 2010; Barro et al. 2016; Tadaki et al. 2017). Very compact sizes have also been found in bright sources at centimeter wavelengths (10GHz) (Murphy et al. 2017). In these massive galaxies, while star formation as traced by  $H\alpha$  emission is in extended, rotating disks, the star formation inferred from dust emission is much more centrally concentrated, building their centers (Genzel et al. 2013; Tadaki et al. 2017). This suggests dust-obscured in-situ star formation could be an important formation channel for the dense cores of massive galaxies. With  $M_* \sim 10^{11} M_\odot$  at  $z \sim 2$ , these galaxies are likely to be the progenitors of today’s massive elliptical galaxies. The next key question is how dust-obscured star formation is distributed in the progenitors of today’s  $M^*$  galaxies at the equivalent epoch, pushing dust mapping from the most massive galaxies down to more typical galaxies.

It remains uncertain which processes are responsible for building bulges in local massive spirals (e.g. Kormendy 2016). Even for the closest, best studied examples of the Milky Way and Andromeda, the fossil record (stellar ages, abundances, dynamics, and structural parameters) points to a first rapid and dissipative formation event followed by secular growth, but the mechanisms involved remain unclear (e.g. Saglia et al. 2010; Courteau et al. 2011; Dorman et al. 2012; Bland-Hawthorn & Gerhard 2016). In recent years, theoretical considerations, numerical simulations, and empirical results on the structure and kinematics of high- $z$  star-forming galaxies have brought forward new bulge formation channels

through efficient disk-internal dissipative processes in the typically gas-rich and turbulent  $z \sim 2$  disks. These  $z \sim 2$  disks typically have baryonic gas mass fractions of  $\sim 30\%-50\%$  (e.g. Tacconi et al. 2013) and intrinsic gas velocity dispersions  $\sim 25-50 \text{ km/s}$  (Genzel et al. 2006; Förster Schreiber et al. 2006, 2009; Kassin et al. 2007; Law et al. 2009; Epinat et al. 2009; Newman et al. 2013; Wisnioski et al. 2015; Stott et al. 2016). In these gas rich-turbulent disks, processes like violent disk instabilities and inward migration of giant star-forming clumps may even lead to “classical” bulges without the need for merger events (e.g. Immeli et al. 2004; Genzel et al. 2008; Zolotov et al. 2015; Bournaud 2016). Though the importance of these processes is debated (e.g. van Dokkum et al. 2015; Lilly & Carollo 2016). With evolving gas inflow rates, sizes, merger rates and surface densities of gas and stars, the physics of disks at  $z \sim 1$  may be very different. In particular, is this how the bulges of  $M^*$  galaxies in the local universe are built? Do they have an equivalent central dust obscured star formation phase before quenching? The potentially complex bulge formation histories underscore the importance of in-situ studies, at epochs when galaxies were most actively forming their stars.

Based on abundance matching arguments, we can link progenitor-descendant populations across cosmic time (e.g. Conroy & Wechsler 2009; van Dokkum et al. 2013; Behroozi et al. 2013; Moster et al. 2013; Papovich et al. 2015; Torrey et al. 2015, 2017; Wellons & Torrey 2017). In this paper we use abundance matching to select a galaxy that based on its stellar mass is likely to have the same mass as Andromeda at  $z = 0$ . Throughout this paper, when we refer to this galaxy as an Andromeda progenitor, we mean that it is likely to be the progenitor of a galaxy which is part of the population of galaxies at  $z = 0$  which have the same mass as Andromeda. The evolution of this population of galaxies inferred from abundance matching is shown in Fig.1. Andromeda has a stellar mass of  $M_* = 1 - 1.5 \times 10^{11} M_\odot$ ,  $\sim 30\%$  of which is in the bulge (e.g. Geehan et al. 2006; Tamm et al. 2012).  $z \sim 1$  is a crucial epoch for studying bulge growth in these galaxies, with steadily increasing Sérsic indices suggesting significant structural evolution and bulge build-up (e.g van Dokkum et al. 2013; Lang et al. 2014; Papovich et al. 2015). Probably related, the quenched fraction is also increasing during this epoch with the quiescent fraction amongst Andromeda

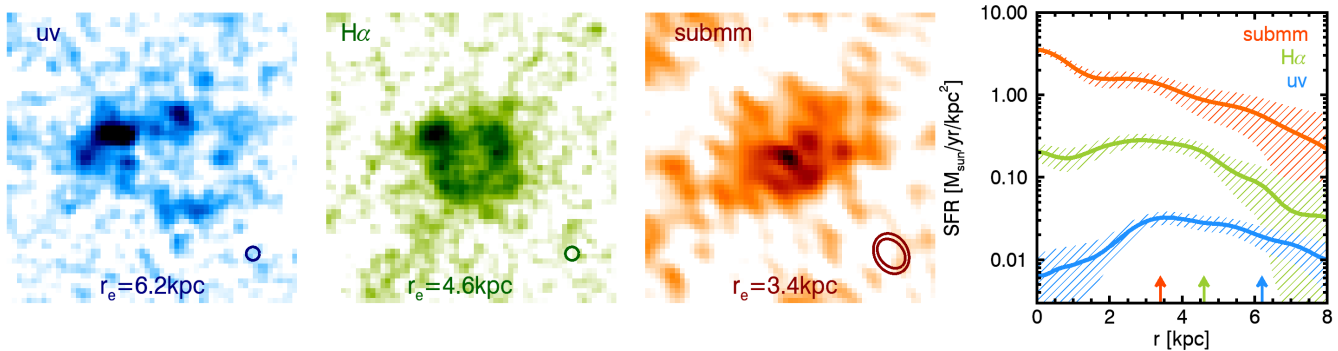


FIG. 2.— Images and surface brightness profiles of the star formation in GOODSN-18574 as traced by rest-UV,  $H\alpha$  from HST and rest-submillimeter (rest- $500\mu\text{m}$ ) from NOEMA. The effective radius in each band is listed at the bottom of the image and shown as an arrow in the plot of the radial profiles. It is clear from the images, surface brightness profiles, and radii that the different tracers of star formation trace very different regions. The star formation gets more compact moving from less to more obscured tracers. The UV is only seen at large radii, the  $H\alpha$  is somewhat more compact but still centrally depressed, while the submm is centrally concentrated. The  $H\alpha$  and even more so the UV, exhibit ring-like structures which are filled in by the dust-obscured star formation as traced by the submm. The dark circles/ellipses in the bottom right corner show the FWHM resolution of the images. The shaded regions reflect the uncertainties due to the noise in the images.

progenitor increases from 47% at  $z = 1.4$  to 70% at  $z = 0.7$  (Papovich et al. 2015).

In this paper, we combine new spatially-resolved 1.1mm (rest- $500\mu\text{m}$ ) data with Hubble Space Telescope  $H\alpha$  maps and UV-NIR imaging to investigate growth patterns in the progenitor of an Andromeda progenitor galaxy at  $z = 1.25$ . This paper is organized as follows. In §2 we describe the target selection, the reduction and analysis of the NOEMA and HST data, and the derivation of spatially-resolved stellar population properties. In §3 we discuss the derivation structural parameters of galaxy growth in rest- $500\mu\text{m}$ ,  $H\alpha$ , UV, rest-optical continuum, and stellar mass. We compare the size, concentration, and radial profiles (SFR and sSFR) in the different tracers as well as the effectiveness of an SED-based dust correction to the  $H\alpha$  and UV data. In §4 we consider structural growth due to star formation in the context of the evolution of central density via the  $\Sigma_1$ - $M_*$  relation and the expected size evolution of Andromeda progenitors. Additionally, we compare the dust continuum size of our Andromeda progenitor to sizes measured for the progenitors of massive elliptical galaxies from Tadaki et al. (2017).

## 2. DATA

### 2.1. Selection

The aim of this initiative was to map the sub-millimeter dust continuum emission in the progenitor of an  $M^*$  galaxy during the time when it was likely to be building its bulge around  $z \sim 1$ . Additionally, the availability of  $H\alpha$  maps at HST resolution for galaxies with  $0.7 < z < 1.5$  allows for a direct comparison between the distribution of obscured and unobscured tracers of star formation. We selected galaxies with stellar masses between the expected stellar masses of Milky Way and Andromeda progenitors in this redshift range based on abundance matching (Moster et al. 2013) (see Fig. 1). To facilitate our exploratory study with NOEMA, we wanted to target a galaxy for which we have sufficiently high S/N to accurately measure the radial distribution and effective radius of the  $H\alpha$  emission for comparison to the rest- $500\mu\text{m}$  data. Finally, we required galaxies to have high  $SFR(IR) > 50 M_\odot/\text{yr}$  based on Spitzer/MIPS and Herschel/PACS plus  $r_e > 0.5''$  to optimize detection and spatially resolved mapping with

NOEMA. Two galaxies were observed with NOEMA for relatively short integrations at low resolution then the one with the stronger detection was chosen for mapping. Thus, the pilot target selected for this exploratory study was GOODSN-18574. This galaxy has  $z=1.248$ ,  $M_* = 6.76 \times 10^{10} M_\odot$ ,  $SFR(IR, H\alpha, UV) = (164, 28, 5) M_\odot/\text{yr}$ <sup>11</sup>, and  $r_e(H_{F160W}) = 0.56''$ , putting this galaxy roughly on the size-mass relation (van der Wel et al. 2014) and  $\sim 0.55$ dex above the SFR-mass relation at this redshift (Whitaker et al. 2014).

### 2.2. NOEMA data reduction and analysis

Dust continuum observations were taken with the IRAM NOthern Extended Millimeter Array (NOEMA) between December 2016 and March 2017. We observed our primary target, GOODSN-18574, for a total on-source integration time of 26 hours in three configurations of the eight antennas: 9h in D, 3h in C and 14h in A (in order from most compact to most extended configuration). Data were taken with the antennas arranged into multiple configurations to efficiently probe emission on multiple scales. We used the compact C and D configurations to probe faint, extended emission (e.g. from a galaxy disk) and the extended A configuration to probe bright, compact emission (e.g. from a galaxy bulge). Observations were carried out in band 3 at 265GHz (1.1 mm), allowing us to measure the rest- $500\mu\text{m}$  dust continuum emission for our target at  $z = 1.248$ . Although this tuning approached the high frequency/short wavelength limit of NOEMA's range where atmospheric transmission is lower, this is compensated for by the increasing brightness of the source moving up the Rayleigh-Jeans tail. The conditions varied but were excellent during observations in A configuration. The primary source of atmospheric opacity, the perceptible water vapor, was low for the A configuration tracks,  $PWV < 1\text{mm}$ , particularly important for these observations which are at the high frequency extrema of NOEMA's range. The noise in the system as reflected in the system temperature was  $T_{\text{sys}} < 200$ . For data taken in the C and D configurations, these values were  $PWV=3\text{--}4\text{mm}$  and  $200 < T_{\text{sys}} < 400$ . Observations of the source were alternated with observations of a bright quasar every twenty min-

<sup>11</sup> These  $H\alpha$  and UV SFRs are not dust-corrected.



FIG. 3.— U-H band imaging with HST. This galaxy exhibits strong color gradients. Going to bluer wave bands, the emission is increasingly suppressed in the center.

utes as a calibrator. The WideX correlator with a bandwidth of 3.6GHz was used for maximal continuum sensitivity.

The data were calibrated following the standard GILDAS/CLIC pipeline performing absolute flux, bandpass, phase, and amplitude calibrations. Additional flagging was done by hand. We combine the amplitudes and  $uv$  distances that comprise the visibility data for all configurations of the antennas into a single dataset and use GILDAS/MAPPING to Fourier Transform the combined data from  $uv$  space to image space using two different weighting schemes. We create one image using ‘Natural’ weighting, in which each visibility is weighted by the inverse of the noise variance to maximize point source sensitivity. Natural weighting yields an image with a synthesized beam size of  $0.4'' \times 0.5''$  and rms noise of  $28 \mu\text{Jy}/\text{beam}$ . We create a second, higher resolution image using ‘Robust’ weighting (with threshold=1) to give increased weight to long baseline data. This image has a beam size of  $0.26'' \times 0.35''$  and rms noise of  $37 \mu\text{Jy}/\text{beam}$ . To improve the resolution in the bright, central region where bulge growth is taking place, we replace the central resolution element of the natural weighted map with the one from the robust weighted map. We note that in this scheme, flux is not conserved. However, this concern is somewhat mitigated because we scale the final image and the surface brightness profile to SFR(IR) (as discussed in § 2.5). This is our imaging procedure for our default image which is shown in Fig. 2. We use a single clean iteration to correct the absolute flux scale of the image but further deconvolution is not warranted by the signal-to-noise ratio of our data. Instead, when necessary, we convolve our comparison data sets with to the resolution of the NOEMA data.<sup>12</sup>

### 2.3. Ancillary data: Hubble imaging and spectroscopy + Spitzer & Herschel photometry

We leverage our NOEMA data using a wealth of ancillary data, which thanks to large investments by the community has been obtained and publicly released. This includes spatially-resolved imaging from HST in eight bands spanning ultra-violet through near-infrared wavelengths as shown in Fig.3. The rest-UV is probed by F275W, F336W (HDUV, Oesch et al., submitted), F435W, F606W, F775W (GOODS Giavalisco et al. 2004). The rest-optical is probed by F125W, F160W (CANDELS Grogin et al. 2011; Koekemoer et al. 2011), and F140W (Skelton et al. 2014, 3D-HST). We use the mosaics provided by the 3D-HST<sup>13</sup> and HDUV<sup>14</sup> teams (Skelton et al. 2014, Oesch et al. submitted). The rest-IR is probed by Spitzer/IRAC  $3.6\mu\text{m}$ ,  $4.5\mu\text{m}$ (Ashby et al. 2013);

$5.8\mu\text{m}$ ,  $8\mu\text{m}$  (Dickinson et al. 2003; Ashby et al. 2013); and Herschel/PACS  $70\mu\text{m}$ ,  $100\mu\text{m}$ ,  $160\mu\text{m}$  (PEP Lutz et al. 2011) We note that these rest-IR tracers are not spatially-resolved for galaxies at  $z \sim 1$ .

The redshift of GOODS-N-18574 was derived based on combined constraints from photometry and 3D-HST spectroscopy (Brammer et al. 2012; Momcheva et al. 2016). A stellar mass of  $6.8 \times 10^{10} M_{\odot}$  was computed by fitting a stellar population synthesis model to the observed U- $8\mu\text{m}$  photometry, using Bruzual & Charlot (2003) templates and assuming solar metallicity, a Chabrier (2003) initial mass function, an exponentially declining star formation history, and the Calzetti et al. (2000) dust attenuation law (see Skelton et al. 2014).

We make an  $H\alpha$  map of this galaxy using data from the 3D-HST grism spectroscopic survey (van Dokkum et al. 2011; Brammer et al. 2012; Momcheva et al. 2016). To make the  $H\alpha$  map of GOODS-N-18574 we subtract quantitative models for both the contamination from overlapping spectra of other objects and stellar continuum emission. The continuum model is generated by convolving the best-fit SED with the combined  $J_{F125W}/J_{H_{F140W}}/H_{F160W}$  image and accounts for a spatially-resolved stellar absorption. With a FWHM spectral resolution of  $\sim 100 H\alpha \lambda 6563\text{\AA}$  and  $[\text{N II}] \lambda \lambda 6548 + 6583\text{\AA}$  are blended. To account for the contamination of  $H\alpha$  by  $[\text{N II}]$ , we assume flat radial gradients, scale the measured flux down by a factor of  $H\alpha_{\text{corr}} = H\alpha_{\text{meas}}/1.3$  and adopt  $H\alpha_{\text{corr}}$  as the  $H\alpha$  flux (Wuyts et al. 2014, 2016). For a more detailed description, see Nelson et al. (2016b). We use iraf PSFMATCH to convolve all the HST data to the resolution of the millimeter data.

### 2.4. Spatially-resolved stellar population properties

Spatially resolved maps of stellar mass and E(B-V) made from the eight band HST imaging are shown in Fig. 4. The creation of these maps is covered in detail in Cibinel et al. (2015) but we briefly describe it here for completeness. Image postage stamps are cut from the mosaics in each HST band (Fig. 3). Already from the images in different bands it is clear that this galaxy exhibits strong color gradients: redder in the center and bluer at larger radii. The reddening can be due to age, dust, or both and will affect inferences about the distribution of star formation and stellar mass. Rest-UV colors can be used to help distinguish between the effects of dust and age (see e.g. Liu et al. 2017). Postage stamps are convolved by psf-matching to the resolution of the reddest band ( $H_{F160W}$ , which has the lowest resolution). These images are then adaptively smoothed using Adaptsmooth (Zibetti et al. 2009) requiring  $S/N > 5$  in each spatial bin in the  $H_{F160W}$  image, which has the highest  $S/N$ . A potential cause for concern is that this may result in an additional smoothing in the galaxy center where the surface brightness is changing most rapidly. This concern is alleviated, however, by noting that the center is bright and has high  $S/N$  in  $H_{F160W}$  so no smoothing

<sup>12</sup> As a potentially helpful side note: following the imaging procedure, the interferometric images are in units of Jy/beam. To make the flux scale not beam-size-dependent requires scaling by the beam solid angle for an elliptical gaussian with half power beam width major and minor axes  $a$  and  $b$ :  $\pi ab/(4 \ln 2)$ .

<sup>13</sup> <http://3dhst.research.yale.edu/Data.php>

<sup>14</sup> <http://www.astro.yale.edu/hduv/data.html>



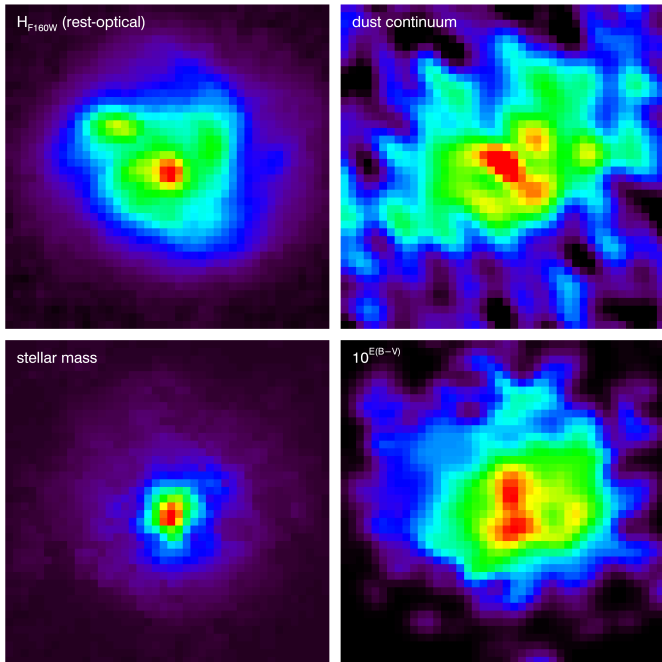


FIG. 4.— The top row shows observed quantities: the HST  $H_{F160W}$  and NOEMA dust continuum images. The bottom row shows maps derived from spatially-resolved stellar population synthesis modeling: maps of stellar mass and dust reddening.

is done inside 6 kpc. The SPS code LePhare (Arnouts et al. 1999; Ilbert et al. 2006) is run on the photometry in each spatial bin using the Bruzual & Charlot (2003) synthetic spectral library, a Chabrier (2003) IMF, a Calzetti et al. (2000) dust law with  $0 < E(B-V) < 0.9$  mag, and three metallicity values ( $Z = 0.2, 0.4, 1 Z_{\odot}$ ). We adopt a delayed exponential star formation history  $(t/\tau^2)\exp(-t/\tau)$  with a characteristic timescale  $\tau$  with 22 values between 0.01 and 10 Gyr and a minimum age of 100 Myr. This method is qualitatively similar to that described in Wuyts et al. (2012) and Lang et al. (2014). Despite using slightly different assumptions and different SPS codes, within 8 kpc, the stellar mass maps from these two methods are typically the same to within 20%.

### 2.5. Star formation indicators

Fig. 2 shows the three different tracers of star formation we have for GOODS-N-18574: UV,  $H\alpha$  and submm. First, the rest-UV (1216-3000Å) traces emission from stars with lifetimes  $< 100$  Myr and the following can be used to scale the UV luminosity to a star formation rate on this timescale:

$$SFR(UV) = 2.40 \times 10^{-10} L_{UV} [L_{\odot}]$$

$L(UV)$  is the total UV luminosity from 1216–3000Å computed by scaling the rest-frame 2800Å luminosity (Bell et al. 2005; Whitaker et al. 2014). We probe the rest-UV emission with the HST/ $B_{F435W}$  filter, corresponding to rest-frame 2040Å, near the center of the optimal wavelength range for determining UV-based star formation rates. We then scale this image to the integrated UV SFR. Because of the short wavelength, this emission is highly attenuated by dust.

Second, the  $H\alpha$  recombination line re-emits emission shortward of the Lyman limit, providing a probe of stars with lifetimes  $< 10$  Myr. To scale the  $H\alpha$  luminosity to a star formation rate, we use the relation presented in Kennicutt (1998)

adapted from a Salpeter to a Chabrier (2003) IMF:

$$SFR(H\alpha) = 1.7 \times 10^{-8} L_{H\alpha} [L_{\odot}]$$

With a rest wavelength of 6563Å,  $H\alpha$  is less impacted by dust attenuation than the UV but still suffers significant attenuation in dusty galaxies.

Third, the bulk of the bolometric luminosity from young massive stars is absorbed and re-radiated in the infrared, with a peak in emission near 100 $\mu$ m (e.g. Lutz et al. 2016). The total infrared luminosity ( $L(IR)$ ) is computed from Herschel/PACS 160 $\mu$ m (Lutz et al. 2011; Magnelli et al. 2013) using a luminosity-independent template (Wuyts et al. 2011) and scaled to a star formation rate using:

$$SFR(IR) = 1.09 \times 10^{-10} L_{IR} [L_{\odot}]$$

In intermediate- and high- redshift galaxies, this far-IR emission is not resolved with Herschel. The only currently feasible way to resolve long-wavelength dust emission in intermediate- and high-redshift galaxies is using mm/submm interferometers. Here we take advantage of the high resolution and continuum sensitivity of the NOEMA millimeter interferometer to resolve the rest-500 $\mu$ m dust continuum emission. We scale this rest-500 $\mu$ m image to the total SFR(IR) computed from the Herschel/PACS 160 $\mu$ m and use it as a proxy for dust-obscured star formation. In star-forming galaxies, emission at the IR peak is due largely to thermal emission by dust that has been heated by star formation. Our scaling assumes a flat temperature gradient across the galaxy, while in local galaxies typically exhibit negative temperature gradients (i.e. hotter temperatures in the center) (e.g. Engelbracht et al. 2010; Pohlen et al. 2010; Galametz et al. 2012; Hunt et al. 2015). If this were the case in this galaxy, it would suggest that the intrinsic dust-obscured star formation is more centrally concentrated than we infer.

## 3. STRUCTURAL PROPERTIES OF GALAXY GROWTH

Fig. 2 shows the images and radial surface brightness profiles of the different tracers of star formation in GOODS-N-18574. What is immediately clear is that the dust-obscured star formation is more concentrated than the unobscured star formation. In this section we quantify the structural properties of growth in GOODS-N-18574 using the size, concentration, and radial surface brightness profiles. We compare these quantities amongst the different star formation tracers UV,  $H\alpha$ , and dust continuum emission and between stellar mass and rest optical light. By comparing the structural parameters of star formation to those of the stellar mass, we infer how this galaxy is growing through star formation.

### 3.1. Size

We measure the size of the dust continuum emission directly from the visibility data (as shown in Fig. 5). The advantage of fitting the observed visibilities directly in the interferometric  $uv$ -plane, rather than in the image plane is that the uncertainties associated with the complex mathematical transformations performed in the imaging process are removed. In this method, each model flux distribution is convolved with the beam in image space, Fourier Transformed to  $uv$ -space, then resampled to the observed UV baselines. The fitting is performed using a circular gaussian model with the centroid, flux, and full width at half maximum (FWHM) as free parameters. The best fit is then determined by  $\chi^2$  minimization. We

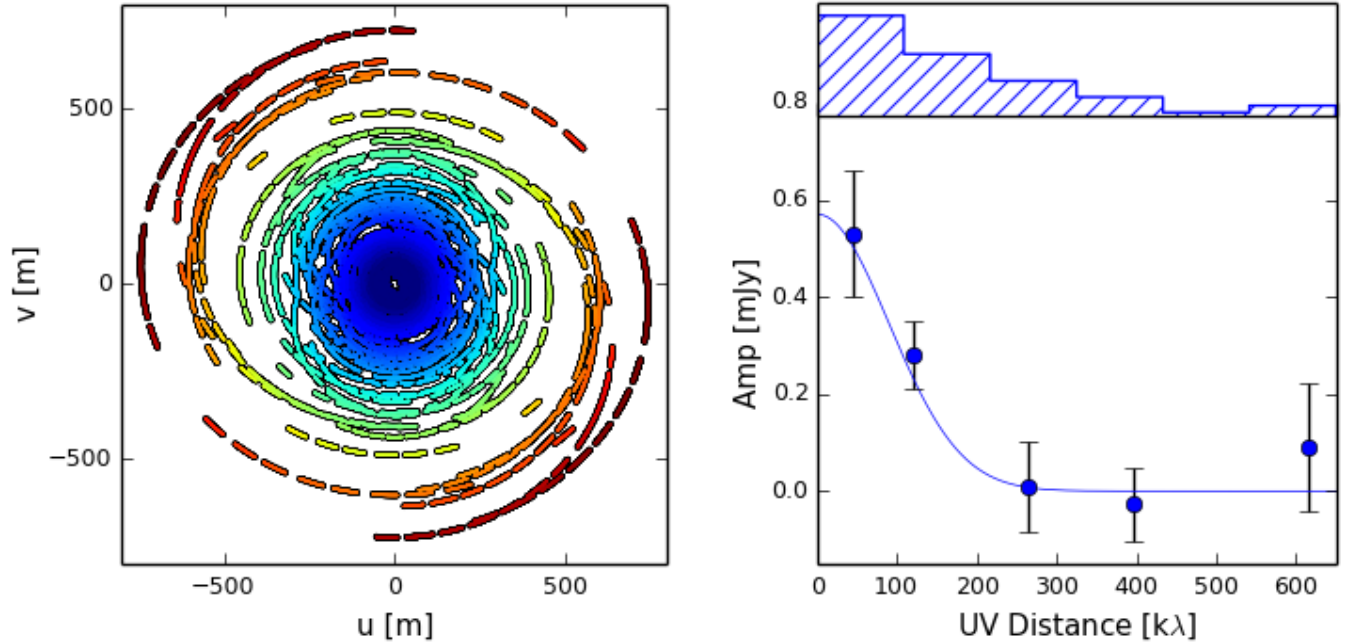


FIG. 5.— We fit the size of the rest-500 $\mu\text{m}$  continuum in the  $uv$  plane. Left: data as a function of position in the  $uv$  plane. Right: Data averaged in bins of UV distance, with the fit overplotted as a line. The histogram reflects the quantity of data in each bin of  $uv$  distance

find  $r_e(\text{rest-}500\mu\text{m}) = 3.4 \pm 0.7$  kpc. We obtain this fit using the GILDAS/Mapping routine UVFIT, results are the same within the errors when using CASA/UVMODELFIT. If we instead fit with the physically more well-motivated exponential, we find  $r_e(\text{rest-}500\mu\text{m}) = 3.7$  kpc, well within the uncertainties of the fit.

We measure sizes for the rest-optical data (specifically  $JH_{F140W}$  tracing the  $\lambda_{\text{rest}} = 6220\text{\AA}$  light) and stellar mass map by fitting Sérsic models (Sérsic 1968) convolved with the point spread function (PSF) of the images using GALFIT (Peng et al. 2002). For the mass map, we used the empirical  $H_{F160W}$  PSF (the PSF to which all images that go into making the mass map are convolved). For the  $JH_{F140W}$  image we use the interlaced PSF generated by Tiny Tim (Krist 1995). We determine error bars by performing Monte Carlo simulations forcing the values of the centroid and Sérsic index to remain fixed. We vary the centroid within a  $0.2''$  box and the Sérsic index by  $\pm 50\%$ . Neither the  $H\alpha$  nor UV emission are centrally peaked so they are poorly fit by Sérsic models and correcting for the PSF is unimportant for a determination of the size. Instead, we measure their sizes using growth curves. The radial surface brightness profiles are measured in finely sampled circular apertures and  $r_e$  is the radius at which the enclosed flux is 50% of the total. We determine the uncertainties on the growth curve sizes by taking the standard deviation of Monte Carlo simulations run varying the centroid within a box of  $0.2''$ . We find  $r_e(\text{optical}) = 4.7 \pm 0.2$  kpc,  $r_e(\text{mass}) = 2.9 \pm 0.2$  kpc,  $r_e(\text{UV}) = 6.2 \pm 0.2$  kpc, and  $r_e(\text{H}\alpha) = 4.8 \pm 0.2$  kpc,

With regard to star formation tracers, we find  $r_e(\text{UV}) > r_e(\text{H}\alpha) > r_e(\text{submm})$ . That is, the submm, which traces dust-obscured star formation, is the most compact, the UV, which traces unobscured star formation is most extended, and the  $H\alpha$  which is somewhat less impacted by dust attenuation is in the middle. Given that the UV size is nearly twice that of the submm size, it is clear that gradients in dust attenuation play a significant role in this galaxy. The true distribution of

star formation is more compact than would be inferred based on the  $H\alpha$  or UV emission alone. If GOODSN-18574 has a negative temperature gradient, then the dust-obscured star formation would be even more compact than we measure.

We find that the stellar mass distribution inferred from spatially-resolved SED fitting is more compact than the rest-optical light. Comparing the distribution of star formation to existing stellar mass, we find  $r_e(\text{UV}) > r_e(\text{H}\alpha) \geq r_e(\text{optical}) > r_e(\text{submm}) \geq r_e(\text{mass})$ . Thus, the dust emission is similar to or more extended than the stellar mass. Even though the star formation is more compact than the unobscured tracers suggest, the mass is also more compact than the rest-optical light suggests. This galaxy is still building between self-similarly and inside-out (i.e. growing larger in size due to star formation).

### 3.2. Concentration

We compute the concentration by dividing the flux in a central aperture by the total flux. As an estimate of concentration we measure  $C = F(r < 0.3'') / F(r < 1'')$ , a number which is related to the bulge to total ratio in a galaxy (e.g. Abraham et al. 1994, 1996; Lotz et al. 2004). We choose this definition of concentration to optimally use the information content of the new interferometric millimeter data presented in this paper. We measure  $F(r < 0.3'')$  from our higher resolution, lower sensitivity image and  $F(r < 1'')$  from our lower resolution, higher sensitivity image. We find a concentration of  $C(\text{rest-}500\mu\text{m}) = F(r < 0.3'') / F(r < 1'') = 0.17$ . We can compare this concentration to the concentration of other star formation tracers  $H\alpha$  and UV as well as to optical emission and stellar mass. We measure concentrations in an identical way on the convolved HST data and find  $C(\text{H}\alpha) = 0.04$ ,  $C(\text{UV}) = 0.02$ ,  $C(\text{optical}) = 0.10$ ,  $C(\text{mass}) = 0.22$ .

Analogously to the trends for effective radius we find  $C(\text{UV}) < C(\text{H}\alpha) < C(\text{optical}) < C(\text{rest-}500\mu\text{m}) < C(\text{mass})$ . The millimeter emission is more concentrated than the  $H\alpha$  emission which is more concentrated than the UV emission.

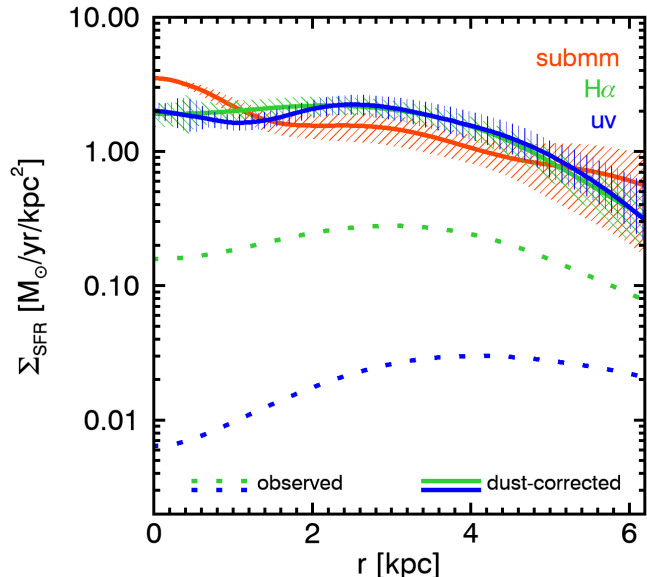


FIG. 6.— Here we show the radial distribution of star formation inferred from the unobscured tracer  $H\alpha$  alone (light blue), corrected for dust attenuation using the rest UV-optical SED (blue), and combining the obscured plus unobscured tracers rest- $500\mu\text{m}$  and  $H\alpha$  (red) as described in §3.3. After correcting for dust using the SED  $A_V$  map, the  $H\alpha$  traces the IR fairly well in a radially averaged sense. There does appear to be some excess central emission, however that is too obscured to recover.

The dust obscured star formation is more centrally concentrated than the unobscured star formation: the dust-obscured star formation is growing the bulge. The rest- $500\mu\text{m}$  emission is also more centrally concentrated than the rest-optical emission but not than the stellar mass. Based on comparing the size and concentration of the rest- $500\mu\text{m}$  emission to the rest-optical, which is often taken as a proxy for stellar mass, we would infer that the star formation is more compact than the stellar mass implying that star formation is actually shrinking the effective radius of the galaxy. However, if we instead compare the size and concentration of the rest- $500\mu\text{m}$  emission to those of the modeled stellar mass map, this is not the case. The bulge of this galaxy is undergoing a period of growth but this growth is not so dramatic that it decreases the effective radius of the galaxy.

### 3.3. Radial profiles of SFR and sSFR

Finally we consider the radial SFR profiles in GOODS-N-18574, comparing the obscured and unobscured tracers of star formation (Fig. 6). We additionally show where this galaxy is growing by comparing the radial distribution of star formation and stellar mass using the specific star formation rate  $sSFR = SFR/M_*$  (Fig. 7). We extract radial profiles from the PSF-matched images of star formation, made as described in §2.5. This galaxy is fairly round ( $b/a = 0.83$  in  $H_{F160W}$ ) so we extract radial profiles in circular apertures centered on the  $H_{F160W}$  flux-weighted centroid (which is also the center of mass).

The radial profiles of star formation are shown in Fig. 6 (as well as Fig. 2). The dust-obscured star formation dominates over the unobscured star formation at all radii. It is roughly an order of magnitude greater than the  $H\alpha$  based star formation rates and nearly two orders of magnitude greater than the UV-based star formation rates. But it is not just an offset between the three tracers, the profiles also have markedly

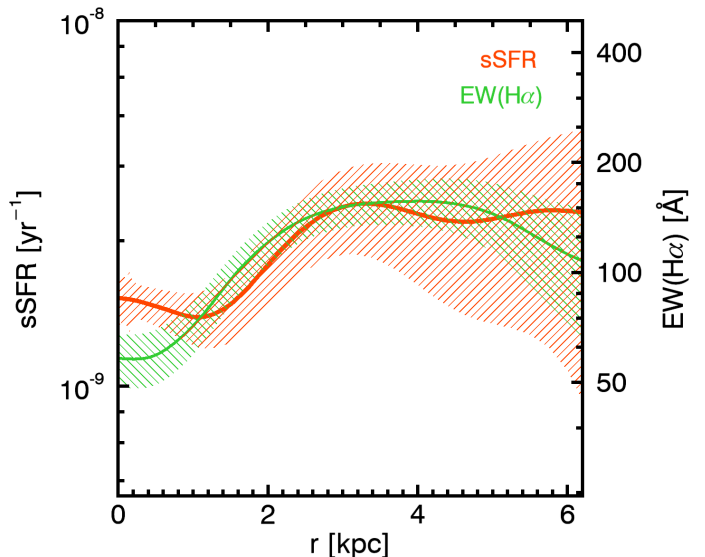


FIG. 7.— Here we show a comparison of the radial  $H\alpha$  equivalent ( $EW(H\alpha)$ ) and specific star formation rate (sSFR) and profiles for GOODS-N-18574. In blue,  $EW(H\alpha)$  reflects the quotient of the  $H\alpha$  and surrounding continuum emission, which is often taken as a proxy for sSFR. In red, the plotted sSFR is the quotient of the SFR traced by the rest- $500\mu\text{m}$  continuum emission and the stellar mass. The sSFR is somewhat higher at large radii than in the center, suggesting the stellar mass is growing more rapidly in the outskirts; the galaxy is building inside-out. The radial behavior of  $EW(H\alpha)$  is fairly similar to the dust-corrected sSFR in this galaxy, meaning that in this galaxy  $EW(H\alpha)$  is a good tracer of the sSFR.

different shapes, reflecting the results from simpler size and concentration measurements. While the  $H\alpha$ , and to an even greater extent the UV, are centrally depressed, the dust is centrally peaked. There is significantly more dust-obscured bulge growth than implied by the unobscured tracers.

Clearly, without accounting for dust, the radial distributions of star formation inferred from different tracers are very different. We test using a map of dust attenuation from spatially-resolved SED modeling to correct the  $H\alpha$  and UV emission for the effects of dust. (Note, the SED modeling includes four bands covering rest-NUV-FUV: ACS/F606W & F435W plus UVIS/F336W & F275W.) We use the resulting  $E(B-V)$  map to correct the  $SFR(H\alpha)$  and  $SFR(UV)$  for the effects of dust with:

$$SFR(\text{dustcorr}) = SFR \times 10^{0.4k(\lambda)E(B-V)}$$

where  $k(\lambda)$  is computed using the Calzetti et al. (2000) dust attenuation law at the wavelength of our observations  $k(H\alpha = 6563\text{\AA}) = 3.32$  and  $k(UV = 2040\text{\AA}) = 8.76$ . As our default, we do not include extra attenuation toward HII regions when correcting the  $H\alpha$  but the difference in the profile when adding extra attenuation based on Wuyts et al. (2013) is included in the error bar. Error bars are additionally comprised of the formal error on the SPS fit of the dust attenuation and the noise in the image. The overall star formation scale is set by the integrated  $SFR(IR)$  so this is a test of the radial dust attenuation estimate not the overall scaling.

The dust-corrected radial profiles are shown in Fig. 6. There is surprisingly good agreement between IR and the dust-corrected  $H\alpha$  and UV, especially considering how dramatic the differences were before the dust correction. The exception is the center where there is somewhat more dust-obscured star formation than inferred by the dust-corrected  $H\alpha$  and UV.

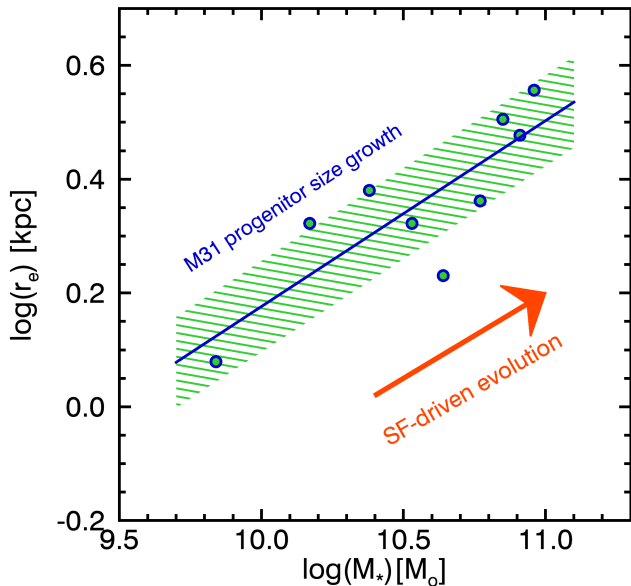


FIG. 8.— Size growth implied by dust-obscured star formation (orange arrow) relative to that empirically derived for M31 progenitors by abundance matching. The points are from Papovich et al. (2015), the blue line shows the best fit, and the green hatched region shows the  $1\sigma$  deviation of the points from the fit. The size growth implied by the dust-obscured star formation is consistent with the expected size growth from population studies.

This suggests that the dust geometry may be more complex than the simple foreground screen assumed for the spatially-resolved SED fitting: if the stars and dust are mixed and some regions have  $\tau \gg 1$ , the rest-optical/UV colors may fail to recover the total quantity of dust-obscured star formation. However, the differences are small and the primary take-away from this exercise is that the dust attenuation map from spatially-resolved SED-fitting to the UV-NIR imaging performs reasonably well correcting for dust in this galaxy.

Fig. 7 shows the radial profile of the specific star formation rate, the star formation rate per unit stellar mass ( $sSFR = SFR/M_*$ ), a reflection of the rate of growth relative to the stellar mass already present. This quantity is derived as the quotient of the star formation rate surface density inferred from the dust continuum emission and the stellar mass map convolved to the same resolution. Also shown in Fig. 7 is the radial  $H\alpha$  equivalent width profile, effectively the scaled quotient of the  $H\alpha$  and respective broad-band emission, which is often used as a tracer of  $sSFR$ . Comparing the radial profiles of  $EW(H\alpha)$  and the dust continuum based  $sSFR$ , we find that inside  $r < 5$  kpc, the two are similar. This similarity suggests that in this galaxy,  $EW(H\alpha)$  is an effective tracer of  $sSFR$  and can be used to determine where a galaxy is growing. We find that the  $sSFR$  increases radially meaning that the galaxy is growing faster in the outskirts than in the center. This positive  $sSFR$  gradient is consistent with the idea that star formation, even after correcting for dust attenuation is more extended than the existing stellar mass. The star formation is making the galaxy larger, growing it from the inside-out.

#### 4. DISCUSSION

##### 4.1. Evolution in Size

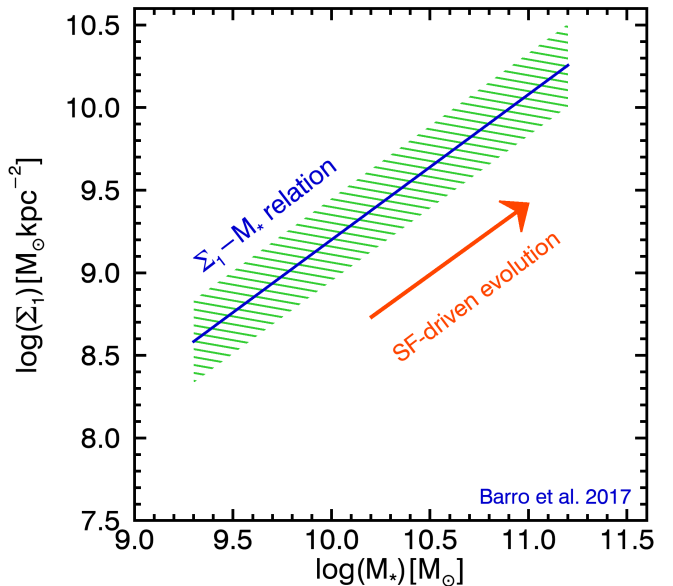


FIG. 9.— Build-up of central stellar mass density implied by dust-obscured star formation (orange arrow) relative to the  $\Sigma_1$ - $M_*$  relation for star-forming galaxies of Barro et al. (2017) (blue line). The green hatched area shows the  $\sigma(\log \Sigma_1) \sim 0.25$  dex observed scatter in the relation. The starting point of the arrow is offset arbitrarily because we measure  $\Sigma(r < 2$  kpc) rather than the  $\Sigma(r < 1$  kpc) that (Barro et al. 2017) measure.

To understand how the observed star formation contributes to structural evolution, we determine to what extent the star formation can account for the structural evolution we expect based on known population-wide scaling relations. First we compare the size growth of GOODS-N-18574 due to star formation to the size growth of Andromeda progenitors empirically derived by Papovich et al. (2015) using abundance matching. With  $SFR = 169 M_\odot/\text{yr}$ , in a time of  $\Delta t = 100$  Myr, this galaxy will grow by  $\Delta M_* = 1.7 \times 10^{10} M_\odot$  (to  $8.5 \times 10^{10} M_\odot$ ). To estimate the size evolution due to this star formation, we scale the best-fit model for the rest- $500\mu\text{m}$  emission to  $\Delta M_*$  and add it to the psf-corrected profile of the existing stellar mass. Thus, we sum the radial profiles  $M_*(r)$  and  $\Delta M_*(r)$  and measure the effective radius of the resulting radial profile using a growth curve. We do not constrain the profile shape so as a check we also do this exercise with Sérsic indices  $n = 0.3 - 3$ .

Our inferred growth trajectory based on dust-obscured star formation is shown as the orange arrow in Fig. 8, while the size evolution of the population of Andromeda progenitors is shown by the points and blue line. The size growth inferred due to star formation is  $\Delta r_e / \Delta M_* = 0.3 \pm 0.1$ . The uncertainty includes results using Sérsic indices  $n = 0.3 - 3$ . The average size growth of the population of the Andromeda progenitors based on a linear fit to the Papovich et al. (2015) size measurements is  $\Delta r_e / \Delta M_* \sim 0.3$ , a growth rate consistent with star forming galaxies in general (van Dokkum et al. 2015). In this galaxy at this time, the expected size growth trajectory can in principle be explained simply by the addition of stellar mass due to star formation (without the need to invoke other processes like merging to redistribute angular momentum after the stars are formed). However, the uncertainty on our rest- $500\mu\text{m}$  size measurement is still large and



including the full range of possibilities in this analysis means that  $\Delta r_e/\Delta M_*$  can formally range from slightly negative to  $\sim 0.5$ , so we caution against interpreting this aspect of our analysis too strongly.

#### 4.2. Evolution in Central Surface Density

We also investigate the evolution of the central stellar mass density of this galaxy, due to dust-obscured star formation. Specifically, we determine to what extent the growth of the central stellar mass density can be accounted for by star formation. To do this, we use the central stellar mass surface density

$$\Sigma_{cen} = M_{cen}/r_{cen}^2$$

where  $M_{cen}$  is the mass contained in a central aperture with radius  $r_{cen}$ . There is a relation between this central stellar mass surface density and the total stellar mass of galaxies  $\Sigma_{cen}-M_*$  (Barro et al. 2017). This relation results from the combined effect of the  $M_*-r_e$  and  $M_*-n_{seraic}$  relations and encapsulates the trend of increasing bulge dominance with increasing stellar mass. The key question is: is the star formation we observe consistent with bulge building, moving the galaxy along this relation?

To answer this question, we compute the trajectory of GOODSN-18574 in the  $\Sigma_{cen}-M_*$  plane due to star formation. If star formation can account for bulge growth, this trajectory should move the galaxy along the observed  $\Sigma_{cen}-M_*$  relation. Investigating this question requires at least a first order correction for the PSF/beam the images. To estimate a correction for the PSF/beam we use Sérsic models as described in Szomoru et al. (2010). Briefly, we use GALFIT best-fit parameters to produce a model for the galaxy that is not convolved with the PSF/beam. We then add the Sérsic model residuals back to this unconvolved model to produce an image that has a first order correction for the PSF. The fits for the HST data are stable and trace the data well. The fit for the NOEMA data is not stable with different initial conditions producing different fits. With the instability of this fit, we tested a large range of fit parameters and found that as long as the central aperture we used was larger than the beam, the measurement was robust against varied fitting parameters. Hence, rather than the 1 kpc aperture used by ( $\Sigma_1$ , Barro et al. 2017), we use a 2 kpc aperture and call this value  $\Sigma_{cen}$ . Our error bar on this measurement includes the full range of beam corrections derived in the fitting.

In Fig. 9, we show a comparison between the population  $\Sigma_1-M_*$  relation found by Barro et al. (2017) (blue line) and the trajectory GOODSN-18574 is moving in this plane due to the star formation we observe (orange arrow). We find that the star formation building this galaxy is moving it along the  $\Sigma_1-M_*$  relation, suggesting that as star formation adds mass to this galaxy, we are witnessing the growth of its bulge. To the best of our information in this galaxy, star formation can build a bulge consistent with the structural relation of star forming galaxies at this epoch.

#### 4.3. Comparison to elliptical progenitors

In addition to placing the dust-obscured star formation in GOODSN-18574 in the context of structural growth, we also compare it to other dust continuum size measurements at intermediate redshift. In particular we consider the growth patterns in this Andromeda progenitor at  $z \sim 1$  to those in massive elliptical progenitors at  $z \sim 2$ . We compare to Tadaki et al. (2017) who present size measurements for H $\alpha$ -selected

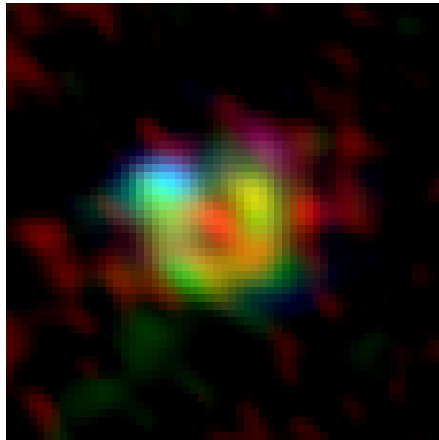


FIG. 10.— Three color image of star formation with UV in blue, H $\alpha$  in green, and rest-500 $\mu$ m in red. The three different tracers trace distinctly different regions of the galaxy.

galaxies with  $M_* > 10^{11}$  at  $z = 2.19$  and  $z = 2.53$ . No lower mass galaxies were detected with sufficient fidelity to measure a size hence there are no size measurements for galaxies with  $M_* < 10^{11}$ . Barro et al. (2016) also studied dust continuum sizes in massive galaxies at  $z \sim 2$ . However, we do not include them here as they were specifically selected to be compact in optical light, which complicates the comparison.

First we compare rest-optical and dust continuum sizes To probe similar rest-optical wavelengths we use  $H_{F160W}$  sizes for the massive comparison sample of galaxies at  $z \sim 2$  and the  $J_{F125W}$  size for GOODSN-18574 at  $z = 1.25$ , corresponding to rest wavelengths of  $\sim 5000\text{\AA}$  and  $5900\text{\AA}$  respectively (van der Wel et al. 2014, from CANDELS). As shown in the left panel of Fig. 11, in all galaxies, the dust continuum is more compact than the rest-optical. This means that all galaxies studied here display significant dust gradients, and likely dust attenuation gradients, although the latter depends on the geometry of the dust. In GOODSN-18574 the submm size is more compact than the optical size by a factor of  $r_e(optical)/r_e(submm) = 1.4$ ; amongst the massive,  $z \sim 2$  comparison sample, it is on average a factor of 2 ( $r_e(optical)/r_e(submm) = 2.0$ ). Relative to the rest-optical, the dust continuum in GOODSN-18574 is less dramatically compact than in the massive elliptical progenitors; it is similar to the galaxies of Tadaki et al. (2017) with the most extended dust continuum emission.

Second, we compare the rest-optical and stellar mass sizes. While the dust continuum is nearly always more compact than the rest-optical emission, if these galaxies have color gradients, they will also have  $M/L$  gradients. Fig. 11 shows  $r_e(M_*)$  vs.  $r_e(light)$  for the full population of galaxies as computed in Lang et al. (2014). This shows that the effective radius is almost always smaller in mass than in light: the stellar mass is nearly always more compact than the rest-optical light.

Finally, we compare the dust continuum and stellar mass sizes. The top right panel of Fig. 11 shows  $r_e(submm)$  vs.  $r_e(M_*)$  for all galaxies for which we have a measurement of the stellar mass effective radius. GOODSN-18574 has  $r_e(submm) > r_e(M_*)$  as do 3/7 galaxies in the sample of Tadaki et al. (2017), while the remaining 4/7 of galaxies in this sample have  $r_e(submm) < r_e(M_*)$ . At face value this means there

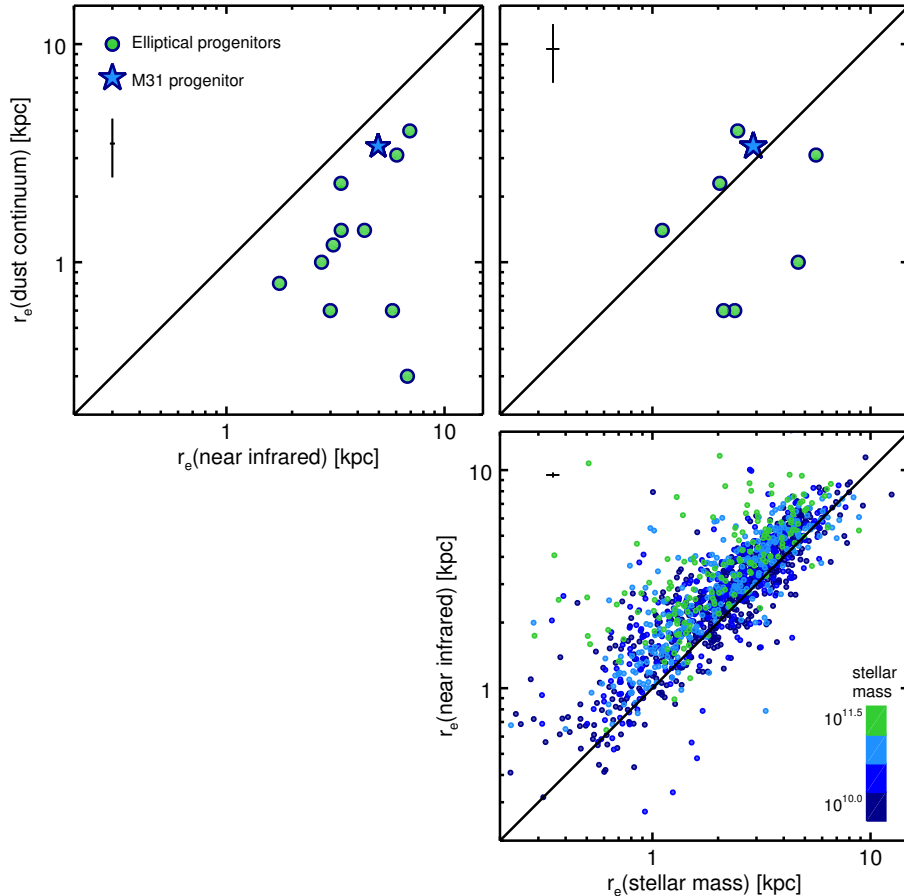


FIG. 11.— Size comparison of the M31 progenitor GOODSN-18574 ( $M_* = 6.76 \times 10^{10} M_\odot$  at  $z=1.25$ ) and the massive elliptical galaxy progenitors of Tadaki et al. (2017) ( $M_* > 1 \times 10^{11} M_\odot$  at  $z=[2.19, 2.53]$ ). The left panel shows that in all the galaxies, the dust continuum is more compact than the near infrared (rest-optical) continuum emission. The bottom right panel shows that in most galaxies with  $M > 1.6 \times 10^{10}$  at  $1 < z < 2.5$ , the stellar mass is more compact than the near infrared continuum emission. The top right panel shows that in roughly half the galaxies in these studies the submm is more compact than the stellar mass and in half it is more extended. Taken at face value, this would suggest that half the galaxies are growing more compact due to star formation and half are staying the same size or growing slightly larger. However, the very high central dust column densities may result in the central stellar mass densities being underestimated. This would mean that the stellar mass sizes are in fact smaller than plotted here, moving the points to the left. Note that four galaxies are not present here because we did not conduct spatially-resolved mass modeling for galaxies with  $H_{F160W} > 23.5$  (see Wuyts et al. 2012; Lang et al. 2014). The crosses in the upper left corner of each plot show the measurement uncertainty. For the near infrared and dust continuum radii, this is the average uncertainty from van der Wel et al. (2014) and Tadaki et al. (2017) respectively. For the stellar mass, this is the fit uncertainty measured for GOODSN-18574. However, with high dust column densities, the systematic uncertainty on the stellar mass sizes is larger.

is a mix of dust continuum sizes, both larger and smaller than the stellar mass sizes. Taking the sub-millimeter emission as a proxy for star formation,  $r_e(\text{submm}) < r_e(M_*)$  could be explained by galaxies undergoing a compaction event in which their dense central regions are grown by a dissipative event which brings gas to the center inducing central star formation (e.g. Dekel & Burkert 2014; Zolotov et al. 2015). On the other hand,  $r_e(\text{submm}) > r_e(M_*)$  most simply implies that at the time of observation, the galaxy is building inside out, with star formation increasing the effective radius (e.g. Nelson et al. 2012; van Dokkum et al. 2015). If these interpretations are correct, then of the galaxies discussed here, roughly half are in the process of undergoing a compaction event and half are growing inside out. Statistics cannot be drawn from one galaxy, however, that GOODSN-18574 does not show evidence for compaction could reflect the theoretical argument that compaction is more common in high mass galaxies at high redshift when gas surface densities were higher.

One important note here is that given the high dust columns

toward the centers of the massive  $z \sim 2$  galaxies implied by the submm data, the expected dust attenuation is very high. Consequently, the central stellar mass surface density inferred based on rest-UV/optical data may be too low, meaning the stellar mass effective radii may also be smaller than measured. If this were in fact the case, the effect in the top right panel of Fig. 11 would be to shift points to the left: a higher fraction of galaxies may in reality have  $r_e(\text{submm}) > r_e(M_*)$  and be growing inside-out.

## 5. SUMMARY

In this paper we investigate dust-obscured bulge growth in an Andromeda progenitor at  $z = 1.25$ . We combine new millimeter dust continuum mapping from the NOEMA interferometer with  $H\alpha$ , UV, and stellar mass maps to place constraints on the formation pathways for bulge-disk systems.

GOODSN-18574 displays a ring in  $H\alpha$  and UV emission, implying the central star formation is strongly centrally suppressed in an absolute sense. However, when imaged at mil-

limeter wavelengths, we instead see centrally concentrated dust-continuum emission, meaning this ring in unobscured star formation is likely filled in by dust-obscured star formation. This suggests that in this galaxy, the ring observed in  $H\alpha$  and UV emission is caused by dust-obscuration rather than centrally suppressed star formation. This is the main result of this paper: the bulge of this galaxy is building by dust-obscured star formation.

To quantify this bulge building, we determine what fraction of the bulge growth underway at  $z \sim 1$  can be accounted for by the star formation we observe. In §4.2 we derive the quantity of bulge growth relative to disk growth that would be required in order for a galaxy to remain on the scaling relation between central stellar mass surface density (as a proxy for bulge mass) and total stellar mass. We find that the dust-obscured star formation we observe would move this galaxy along a trajectory with the same slope as this relation. Within the (significant) errors on this measurement, in this galaxy at this epoch, bulge growth can be explained by dust-obscured star formation. This galaxy lies above the main sequence and its optical morphology suggests perhaps that it is undergoing a minor merger and/or have a large clump in the disk. Taken together, our observations are consistent with a picture in which merging and disk instabilities drive gas to the center of the galaxy, boosting the global star formation rate, and building the bulge.

The bulge and disk of this galaxy are building simultaneously. Although the bulge growth is dust-obscured, the disk growth is apparent in the rest-500 $\mu$ m,  $H\alpha$ , and UV. Furthermore, while the dust-obscured star formation is more concentrated than the un-obscured star formation, it has a similar or larger size than the stellar mass. The star formation we observe, although the errors are large, is consistent with the expected size evolution of Andromeda progenitors at this epoch, gradually growing larger at a rate of  $\Delta r_e / \Delta M_* \sim 0.3$ .

This is in contrast to the dust continuum measurements of

some massive galaxies at  $z \sim 2$ , which are the putative progenitors of local massive elliptical galaxies. While mm/submm observations reveal dust-obscured bulge/dense core growth for both Andromeda- and massive elliptical progenitors, some of the very massive galaxies at  $z \sim 2$  may actually be getting more compact due to star formation. It is expected that this strong form of compaction is more common at  $z = 2$  than  $z = 1$  due to higher gas fractions and merger rates. However, given the extremely high dust column densities toward the centers of these galaxies, we may be significantly underestimating the central stellar mass surface density already present. If this were the case, these galaxies would not in fact be undergoing compaction in the sense of physically shrinking in radius. Spatially resolved stellar population synthesis modeling which takes into account resolved millimeter constraints is needed before this can be definitively answered.

The ability to map the structural growth of galaxies provides powerful constraints on the physical drivers of their evolution. This requires maps of star formation and stellar mass which account for the effects of dust and age. In this paper we showed that dust-obscured star formation can play a key role in our understanding of the structural evolution of galaxies. Looking ahead, to really determine how galaxies are growing and whether dust-obscured star formation is responsible for the building of bulges and dense cores requires dust continuum mapping with high spatial resolution statistical samples of galaxies at a range of redshifts beyond  $z > 1$  and across the SFR- $M_*$  plane. Because the progenitors of galaxies like the Milky Way and Andromeda have lower masses, and correspondingly lower gas masses and metallicities, longer integration times will be needed to map them – but these measurements are key to understand how bulges build. Additionally, high resolution mapping of molecular gas kinematics will be essential to placing more stringent constraints on the physical processes responsible for building the dense centers of galaxies.

## REFERENCES

- Abraham, R. G., Tanvir, N. R., Santiago, B. X., et al. 1996, *MNRAS*, 279, L47
- Abraham, R. G., Valdes, F., Yee, H. K. C., & van den Bergh, S. 1994, *ApJ*, 432, 75
- Arnouts, S., Cristiani, S., Moscardini, L., et al. 1999, *MNRAS*, 310, 540
- Ashby, M. L. N., Willner, S. P., Fazio, G. G., et al. 2013, *ApJ*, 769, 80
- Barro, G., Kriek, M., Pérez-González, P. G., et al. 2016, *ApJ*, 827, L32
- Barro, G., Faber, S. M., Koo, D. C., et al. 2017, *ApJ*, 840, 47
- Behroozi, P. S., Wechsler, R. H., & Conroy, C. 2013, *ApJ*, 770, 57
- Bell, E. F., Papovich, C., Wolf, C., et al. 2005, *ApJ*, 625, 23
- Bland-Hawthorn, J., & Gerhard, O. 2016, *ARA&A*, 54, 529
- Bournaud, F. 2016, in *Astrophysics and Space Science Library*, Vol. 418, Galactic Bulges, ed. E. Laurikainen, R. Peletier, & D. Gadotti, 355
- Brammer, G. B., van Dokkum, P. G., Franx, M., et al. 2012, *ApJS*, 200, 13
- Bruzual, G., & Charlot, S. 2003, *Monthly Notices of the Royal Astronomical Society*, 344, 1000
- Calzetti, D., Armus, L., Bohlin, R. C., et al. 2000, *ApJ*, 533, 682
- Chabrier, G. 2003, *PASP*, 115, 763
- Cibinel, A., Le Floch, E., Perret, V., et al. 2015, *ApJ*, 805, 181
- Conroy, C., & Wechsler, R. H. 2009, *ApJ*, 696, 620
- Courteau, S., Widrow, L. M., McDonald, M., et al. 2011, *ApJ*, 739, 20
- Dekel, A., & Burkert, A. 2014, *MNRAS*, 438, 1870
- Dickinson, M., Giavalisco, M., & GOODS Team. 2003, in *The Mass of Galaxies at Low and High Redshift*, ed. R. Bender & A. Renzini, 324
- Dorman, C. E., Guhathakurta, P., Fardal, M. A., et al. 2012, *ApJ*, 752, 147
- Engelbracht, C. W., Hunt, L. K., Skibba, R. A., et al. 2010, *A&A*, 518, L56
- Epinat, B., Contini, T., Le Fèvre, O., et al. 2009, *Astronomy and Astrophysics*, 504, 789
- Förster Schreiber, N. M., Genzel, R., Lehnert, M. D., et al. 2006, *ApJ*, 645, 1062
- Förster Schreiber, N. M., Genzel, R., Bouché, N., et al. 2009, *ApJ*, 706, 1364
- Galametz, M., Kennicutt, R. C., Albrecht, M., et al. 2012, *MNRAS*, 425, 763
- Geehan, J. J., Fardal, M. A., Babul, A., & Guhathakurta, P. 2006, *MNRAS*, 366, 996
- Genzel, R., Tacconi, L. J., Eisenhauer, F., et al. 2006, *Nature*, 442, 786
- Genzel, R., Burkert, A., Bouché, N., et al. 2008, *ApJ*, 687, 59
- Genzel, R., Tacconi, L. J., Kurk, J., et al. 2013, *ApJ*, 773, 68
- Giavalisco, M., Ferguson, H. C., Koekemoer, A. M., et al. 2004, *ApJ*, 600, L93
- Grogin, N. A., Kocevski, D. D., Faber, S. M., et al. 2011, *ApJS*, 197, 35
- Hunt, L. K., Draine, B. T., Bianchi, S., et al. 2015, *A&A*, 576, A33
- Ilbert, O., Arnouts, S., McCracken, H. J., et al. 2006, *A&A*, 457, 841
- Immeli, A., Samland, M., Westera, P., & Gerhard, O. 2004, *ApJ*, 611, 20
- Kassin, S. A., Weiner, B. J., Faber, S. M., et al. 2007, *ApJ*, 660, L35
- . 2012, *ApJ*, 758, 106
- Kennicutt, Jr., R. C. 1998, *ARA&A*, 36, 189
- Koekemoer, A. M., Faber, S. M., Ferguson, H. C., et al. 2011, *ApJS*, 197, 36
- Kormendy, J. 2016, in *Astrophysics and Space Science Library*, Vol. 418, Galactic Bulges, ed. E. Laurikainen, R. Peletier, & D. Gadotti, 431
- Krist, J. 1995, in *Astronomical Society of the Pacific Conference Series*, Vol. 77, *Astronomical Data Analysis Software and Systems IV*, ed. R. A. Shaw, H. E. Payne, & J. J. E. Hayes, 349
- Lang, P., Wuyts, S., Somerville, R. S., et al. 2014, *ApJ*, 788, 11
- Law, D. R., Steidel, C. C., Erb, D. K., et al. 2009, *ApJ*, 697, 2057
- Lilly, S. J., & Carollo, C. M. 2016, *ApJ*, 833, 1
- Liu, F. S., Jiang, D., Guo, Y., et al. 2016, *ApJ*, 822, L25
- Liu, F. S., Jiang, D., Faber, S. M., et al. 2017, *ApJ*, 844, L2
- Lotz, J. M., Primack, J., & Madau, P. 2004, *AJ*, 128, 163
- Lutz, D., Poglitsch, A., Altieri, B., et al. 2011, *A&A*, 532, A90
- Magnelli, B., Popesso, P., Berta, S., et al. 2013, *A&A*, 553, A132
- Momcheva, I. G., Brammer, G. B., van Dokkum, P. G., et al. 2016, *ApJS*, 225, 27
- Moster, B. P., Naab, T., & White, S. D. M. 2013, *MNRAS*, 428, 3121
- Murphy, E. J., Momjian, E., Condon, J. J., et al. 2017, *ApJ*, 839, 35
- Nelson, E. J., van Dokkum, P. G., Brammer, G., et al. 2012, *ApJ*, 747, L28
- Nelson, E. J., van Dokkum, P. G., Momcheva, I., et al. 2013, *The Astrophysical Journal*, 763, L16

- Nelson, E. J., van Dokkum, P. G., Momcheva, I. G., et al. 2016a, *ApJ*, 817, L9
- Nelson, E. J., van Dokkum, P. G., Förster Schreiber, N. M., et al. 2016b, *ApJ*, 828, 27
- Newman, S. F., Genzel, R., Förster Schreiber, N. M., et al. 2013, *ApJ*, 767, 104
- Papovich, C., Labbé, I., Quadri, R., et al. 2015, *The Astrophysical Journal*, 803, 26
- Peng, C. Y., Ho, L. C., Impey, C. D., & Rix, H.-W. 2002, *AJ*, 124, 266
- Pohlen, M., Cortese, L., Smith, M. W. L., et al. 2010, *A&A*, 518, L72
- Reddy, N. A., Erb, D. K., Pettini, M., Steidel, C. C., & Shapley, A. E. 2010, *ApJ*, 712, 1070
- Reddy, N. A., Steidel, C. C., Fadda, D., et al. 2006, *ApJ*, 644, 792
- Reddy, N. A., Oesch, P. A., Bouwens, R. J., et al. 2017, *ArXiv e-prints*, arXiv:1705.09302
- Saglia, R. P., Fabricius, M., Bender, R., et al. 2010, *A&A*, 509, A61
- Sérsic, J. L. 1968, *Atlas de galaxies australes*, ed. Sérsic, J. L.
- Skelton, R. E., Whitaker, K. E., Momcheva, I. G., et al. 2014, *ApJS*, 214, 24
- Stott, J. P., Swinbank, A. M., Johnson, H. L., et al. 2016, *MNRAS*, 457, 1888
- Szomoru, D., Franx, M., van Dokkum, P. G., et al. 2010, *ApJ*, 714, L244
- Tacconi, L. J., Genzel, R., Smail, I., et al. 2008, *ApJ*, 680, 246
- Tacconi, L. J., Genzel, R., Neri, R., et al. 2010, *Nature*, 463, 781
- Tacconi, L. J., Neri, R., Genzel, R., et al. 2013, *ApJ*, 768, 74
- Tadaki, K.-i., Genzel, R., Kodama, T., et al. 2017, *ApJ*, 834, 135
- Tamm, A., Tempel, E., Tenjes, P., Tihhonova, O., & Tuvikene, T. 2012, *A&A*, 546, A4
- Torrey, P., Wellons, S., Ma, C.-P., Hopkins, P. F., & Vogelsberger, M. 2017, *MNRAS*, 467, 4872
- Torrey, P., Wellons, S., Machado, F., et al. 2015, *MNRAS*, 454, 2770
- van der Wel, A., Franx, M., van Dokkum, P. G., et al. 2014, *The Astrophysical Journal*, 788, 28
- van Dokkum, P. G., Brammer, G., Fumagalli, M., et al. 2011, *ApJ*, 743, L15
- van Dokkum, P. G., Leja, J., Nelson, E. J., et al. 2013, *The Astrophysical Journal*, 771, L35
- van Dokkum, P. G., Nelson, E. J., Franx, M., et al. 2015, *ApJ*, 813, 23
- Wang, W., Faber, S. M., Liu, F. S., et al. 2017, *MNRAS*, 469, 4063
- Wellons, S., & Torrey, P. 2017, *MNRAS*, 467, 3887
- Whitaker, K. E., van Dokkum, P. G., Brammer, G., & Franx, M. 2012, *ApJ*, 754, L29
- Whitaker, K. E., Franx, M., Leja, J., et al. 2014, *ApJ*, 795, 104
- Wisnioski, E., Glazebrook, K., Blake, C., et al. 2011, *Monthly Notices of the Royal Astronomical Society*, 417, 2601
- Wisnioski, E., Förster Schreiber, N. M., Wuyts, S., et al. 2015, *ApJ*, 799, 209
- Wuyts, E., Kurk, J., Förster Schreiber, N. M., et al. 2014, *ApJ*, 789, L40
- Wuyts, E., Wisnioski, E., Fossati, M., et al. 2016, *ApJ*, 827, 74
- Wuyts, S., Förster Schreiber, N. M., Lutz, D., et al. 2011, *ApJ*, 738, 106
- Wuyts, S., Förster Schreiber, N. M., Genzel, R., et al. 2012, *ApJ*, 753, 114
- Wuyts, S., Förster Schreiber, N. M., Nelson, E. J., et al. 2013, *ApJ*, 779, 135
- Zibetti, S., Charlot, S., & Rix, H.-W. 2009, *MNRAS*, 400, 1181
- Zolotov, A., Dekel, A., Mandelker, N., et al. 2015, *MNRAS*, 450, 2327